Enhancing Flow Batteries: Topology Optimization of Electrode Porosity and Shape Optimization of Cell Design

Amadeus Wolf,* Jens Noack, Mathias J. Krause, and Hermann Nirschl

This research focuses on the improvement of porosity distribution within the electrode of an all-vanadium redox flow battery (VRFB) and on optimizing novel cell designs. A half-cell model, coupled with topology and shape optimization framework, is introduced. The multiobjective functional in both cases aims to minimize pressure drop while maximizing reaction rate within the cell. Topology optimization results reveal dependencies on initial value, porosity constraint, and flow rate. The distribution with lower porosity is preferred downstream of the inlet manifold. This design enhances active surface area, thus facilitating more effective conversion of incoming educts and improving mass transport of products. Compared to homogeneous electrodes, two-part design demonstrates superior performance at specific porosity values. For combined porosities of 0.7 and 0.95, optimized distribution results in 81 % reduction in pressure drop, while conversion rate decreases by 7%. As regards various cell designs, optimization suggests a need to reconsider the vertical format of a rectangular cell. Horizontal cells are favored for nearly all porosities and flow rates. Trapezoidal and radial designs characterized by reduced downstream cross sections lead to higher pressure drops and are not preferred. This work provides further valuable insight into optimizing VRFB electrodes and challenges conventional cell design assumptions.

1. Introduction

As renewable energy technology advances, the need for large-scale energy storage becomes crucial to ensure continuous power supply from intermittent renewable sources.[1,2] The flow battery (FB) promises to balance grid demand and supply due to its unique design, to allow for an independent scalability of capacity and power, to be environmentally friendly, and to reach extended life cycles.[3,4] However, its high capital costs and relatively low energy density still inhibit widespread use.[5]

The FB is composed of two independent reservoirs holding separated electrolyte solutions and a stack of electrochemical cells. These incorporate two porous, carbonic electrodes separated by an ion transport membrane. During operation, the electrolytes are pumped through the electrochemical cell, where the redox reaction takes place at the surface of the porous electrodes. Subsequently, the charged or discharged electrolyte circulates back into the respective reservoir.[6,7] The all-vanadium system has been the most studied and developed FB system so far, since it profits from the four stable oxidation states of vanadium and their good solubilities.[8–10]

Simulation methods represent suitable tools for acquiring a deeper understanding of the battery's multifaceted physical processes and for forecasting its performance for a number of operational scenarios. The modeling techniques employed to investigate FB constituents and their performances encompass a broad spectrum of length scales. Shah et al. introduced a dynamic 2D model that integrates mass, momentum, and charge conservation principles, along with a kinetic representation of vanadium reactants.[11] This model was subsequently expanded to also cover thermal effects through the inclusion of an energy balance equation.[12] Furthermore, gassing side reactions like hydrogen evolution and oxygen evolution were taken into account.[13] Shah et al. also developed a dynamic unit cell model that established a relationship between process time, conditions, and state of charge.[14] Building upon Shah's transient 2D models, Ma et al. extended the stationary 2D cell model previously proposed by You et al.[15] to a steady-state 3D model for the negative half-cell of a (VRFB).[16] Subsequently, other researchers adapted this model to optimize FB featuring flow-through porous electrodes.[17–19]

Topology optimization[20,21] gained importance in recent years and is presently used in various disciplines. Originating from structural mechanics and additive manufacturing,[22–24] this method is also used in fluid dynamics,[25,26] in fuel cell,[27–30] and FB technology. In the latter case, mostly the flow field or manifold of the cell as well as electrode properties are optimized.

A. Wolf, H. Nirschl
Institute for Mechanical Process Engineering and Mechanics
Karlsruhe Institute of Technology
Strasse am Forum 8, 76131 Karlsruhe, Germany
E-mail: amadeus.wolf@kit.edu

J. Noack
Fraunhofer-Institute for Chemical Technology (ICT)
Joseph-von-Fraunhofer-Str. 7, 76327 Pfinztal, Germany

M. J. Krause
Lattice Boltzmann Research Group
Karlsruhe Institute of Technology
Strasse am Forum 8, 76131 Karlsruhe, Germany

Yaji et al.[31] introduced a 2D topology optimization method for the flow fields of the VRFB as a maximization problem of the generation rate of vanadium species. Instead of a electrochemical reaction formulation, a simplified term was used to account for species generation. They identified the interdigitated flow field as the optimized configuration and revealed that the dimensioning of the electrode thickness is affected by porosity and pressure loss settings. Based on this work, Chen et al.[32] applied a 3D topology optimization model for the VRFB using electrochemical Butler–Volmer-type reaction kinetics. They revealed that the interdigitated-type flow field is best under the investigated operating conditions. Beck et al.[33] presented a computational optimization of a VRFB half cell to design 3D porous electrodes composed of unit cells incorporating spatially varying geometries. The porosity was redistributed to minimize power loss within the electrode. They found a variable porosity distribution leading to higher power efficiencies across operating flow directions and currents. Gilmore et al.[34] applied 2D topology optimization to adaptable manifold configurations that can be used for FB among others. They found an experimentally validated and optimal so-called baffle configuration that minimized pressure loss. He et al.[35] developed a 3D VRFB model to understand the effects of the electrode's structural parameters on battery performance. Among other things, they investigated gradient porosity within the electrode and found that large porosity can minimize concentration overpotentials and reduce pressure loss. Roy et al.[36] used density-based topology optimization for the design of porous electrodes in different electrochemical applications. The optimization problem was formulated to minimize energy loss in a half-cell. They found nontrivial optimized designs showing improved performance over monolithic single-porosity electrodes in terms of effective conductivity and energy loss. Lin et al.[37] extended the work from Beck et al.[33] to utilize topology optimization for generating flow field designs with well-defined solid and liquid regions. As pioneers in the field, they devised an optimization strategy using a multiobjective cost function that aims at concurrent minimization of electrical and flow pressure power losses. They found an optimized, interdigitated flow field design with 3D ramp features that lead to a better distribution of reactant and reaction. Charoen-amornkitt et al.[38] developed a topology optimization model of porosity distribution in a reaction-diffusion system. They connected the numerical approach with an entropy generation analysis to obtain a physical understanding. The results showed a slight improvement in maximizing the response within the reactor for 0D and 1D cases, while optimization for higher dimensionalities yielded significant improvements. Wang et al.[39] introduced topology optimization of microchannel reactors using an improved multi-objective algorithm based on the weighted-sum method. They found that geometries and fluid properties have significant impact on the optimal topology for both Newtonian and non-Newtonian fluids.

The porous electrode within an FB is a key component influencing charge and mass transport. Most systems use felt electrodes consisting of carbonized polymer-based fibers of the micrometer scale. For optimal operation, they must provide a large active surface area for the electrochemical reaction, but also high porosity to minimize pressure loss.[40] Hence, optimizing electrode material and design can lead to a significant improvement in performance and cost reduction.[41]

In most modeling approaches, however, the porosity of the electrode is assumed to be homogeneously distributed. In practice, the porosity of the electrode varies locally due to manufacturing tolerances or clamping pressures. According to Guan et al.[42] this results in low-flow-rate regions or dead zones, leading to concentration overpotential or undesirable side reactions. Prumbohm et al.[43] showed that homogenized models cannot be used to predict the partly inhomogeneous flow distribution observed experimentally within the electrode. Recently, Wan et al.[44] presented a method based on nonsolvent-induced phase separation (NIPS), allowing for the consistent production of electrodes without macrovoids and featuring clearly defined porosity gradients across the thickness. They observed that the performance remains consistent regardless of the direction of the porosity gradient and is comparable to that of state-of-the-art electrodes documented in current literature.

As previously noted, the primary emphasis has been on optimizing the flow field, flow rate, and electrode configuration.[37,45–47] The conventional rectangular vertical-format cell design, which is commonly accepted, has seldom been subject to questioning. Gurieff et al.[17] explored novel design concepts for flow-through electrodes, including rectangular, trapezoidal, and radial geometries. These designs aim to enhance velocity from the inlet to the outlet, thereby improving mass transport within the cell. Gurieff et al.[48] also investigated the combination of static mixers within wedge-shaped cells to improve performance. They found a design with a 12% lower pressure drop. Kok et al.[49] investigated the morphology of electrode structures and the cell architecture of a hydrogen–bromine FB with a interdigitated flow-through configuration. They found that the width of the domain is crucial in terms of reaction rate, meaning that the narrowest rib performed best. Meng et al.[50] introduced the first trapezoidal cell design for FB. They used a stepping optimization method to reduce the concentration polarization at constant porosity. They discovered that the novel structure was efficient in improving mass transport and reducing polarization without an increase in energy consumption.

Despite existing research, the optimal porosity distribution within the electrode and optimal geometric dimensions of novel cell designs remain unclear. The question arises whether a homogeneous porosity distribution is ideal. Our study addresses this gap with a twofold objective: First, determining the optimal porosity distribution through topology optimization and second, exploring the existence of an optimal geometry for novel FB cell designs through shape optimization. To achieve this, we introduce a 2D half-cell model of an experimental VRFB, implemented in COMSOL Multiphysics and validated using experimental data. In contrast to prior research that focused on idealized cells, our contribution utilizes an experimentally validated cell model. Moreover, previous work predominantly concentrated on the individual optimization of either total power loss or reaction rate, while our approach formulates a multiobjective functional to simultaneously enhance the reaction rate and reduce pressure drop within the cell. This dual optimization aims to identify the optimal compromise between these opposing factors. While several novel cell designs have been introduced, their optimal geometric dimensions have not
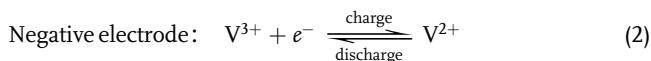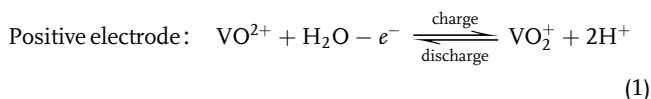
undergone systematic optimization utilizing a multiobjective functional.

In this manuscript, we begin by describing the underlying modeling and optimization approaches in Sections 2 and 3, respectively. The experimental validation of the model is presented in Section 4. In Section 5, we discuss the findings relating to topology optimization of porosity distribution.

The impact of flow rate on the porosity distribution is presented for three distinct intervals and one of the determined distributions is compared against electrodes with homogeneous porosity. Finally, the topology optimization is applied to novel cell geometries introduced by Gurieff et al.[17] These include a rectangular design in a horizontal-format orientation, a trapezoidal design, and a radial design. Additional information about the impact of initial values and single- and multiobjective optimization can be found in the Appendix. A sensitivity study quantifying the influence of model parameters on the porosity distribution and on cell performance is presented as well. In Section 6, shape optimization calculations are conducted for the novel designs to determine their optimal geometric dimensions. Specifically, this involves identifying the optimal height and height-to-width ratio for the rectangular cell, determining the optimal top-to-bottom width ratio for the trapezoidal design, and finding the optimal angle for the radial design.

2. Flow Battery Model

The computational model employed in this study is aimed at a detailed investigation of the half cell of a VRFB. Throughout the charging and discharging processes, the reactions occurring within the porous electrodes can be succinctly represented by the following equations.

$$\text{Positive electrode}: \quad VO^{2+} + H_2O - e^- \underset{\text{discharge}}{\overset{\text{charge}}{\rightleftarrows}} VO_2^+ + 2H^+ \tag{1}$$

$$\text{Negative electrode}: \quad V^{3+} + e^- \underset{\text{discharge}}{\overset{\text{charge}}{\rightleftarrows}} V^{2+} \tag{2}$$

An essential feature of this modeling approach is the incorporation of fluid dynamics and the transport of diluted single species encompassing a homogenized porous medium. Within the scope of this contribution, the model accommodates the conversion of species through the integration of a fundamental reaction term. Consequently, this model is versatile and can be effectively applied to both the cathode and anode half cells alike. Given its straightforward structure, the model exhibits high flexibility, making it applicable to various other systems as well. Unless otherwise specified, the results in this work always refer to the positive half cell. The following section outlines the fundamental physical phenomena underpinning our model, the underlying assumptions guiding our approach, and the definition of the computational domain. It is imperative to note that our model is anchored in the framework of an experimental cell, providing a robust foundation for its applicability and relevance.

2.1. Model Assumptions

The modeling assumptions in the present study are as follows: 1) The electrolyte is modeled as a Newtonian and incompressible fluid with constant density and viscosity. The flow regime is assumed to be laminar and steady state; 2) Constant temperature is assumed, and thermal effects are neglected; 3) The 2D half-cell model is designed to cover the in-plane direction of the cell; 4) Transport and conversion of a single diluted species c are considered, while migration is neglected; 5) The presence of water, hydrogen, and sulfuric acid is not taken into account; and 6) Membrane transport and side reactions are excluded from consideration.

2.2. Governing Equations

The flow of electrolyte through the manifold and the porous electrode is described by the Brinkmann-type Navier–Stokes equations given by

$$\nabla \cdot \mathbf{u} = 0 \tag{3}$$

$$\rho(\mathbf{u} \cdot \nabla)\mathbf{u} = -\nabla p + \mu \nabla^2 \mathbf{u} - \frac{\mu}{K}\mathbf{u} \tag{4}$$

where $\mathbf{u}$ is the velocity, ρ is the density, p is the pressure, μ is the dynamic viscosity of the electrolyte, and K is the permeability. Using the Carman–Kozeny equation, the permeability is expressed as[51]

$$K = \frac{d_f^2 \varepsilon^3}{180(1-\varepsilon)^2} \tag{5}$$

where d_f is the fiber diameter and ε is the porosity. Although this relation actually describes flow through packed beds of spherical particles, it can be used for fibrous porous media in FB application due to the low Reynolds number and comparatively high porosities.[52] The scalar transport of the active species is described using the following steady-state mass balance equation.

$$\mathbf{u} \cdot \nabla c = D_e \nabla^2 c + R_c \tag{6}$$

where c is the concentration of the active species, D_e is the effective diffusion coefficient, and R_c is the volumetric reaction rate. In fact, the migration term is neglected in Equation (6) due to its minor transport effect in in-plane direction.[14,15] To account for the diffusivity in the porous electrode, the diffusion coefficient is calculated according to the Bruggemann correlation[53]

$$D_e = \varepsilon^{1.5} D_c \tag{7}$$

where D_c is the diffusivity. Throughout this study, a fundamental reaction term R_c is used instead of the nonlinear Butler–Volmer equation, to describe the transformation of the active species.[31,54] It is transported by fluid flow and continuously generated until it attains its maximum concentration, labeled as c_{max}. The reaction rate is given by

$$R_c = k_m A_V(c_{max} - c) \tag{8}$$

where k_m is the mass transfer coefficient and A_V is the specific active surface area of the porous electrode. The mass transfer coefficient can be written as[55]

$$k_m = \beta |\mathbf{u}|^\alpha \tag{9}$$

where β and α are empirical parameters depending on the electrochemical system and electrode. In this study, we employ both topology and shape optimization techniques to enhance the design of the FB cell. In the context of topology optimization, the porosity term in Equation (5) is replaced with an optimized porosity ε_{opt}. For shape optimization, the electrode reference domain D, as illustrated in **Figure 1**, is associated with the optimization control variable ψ.

$$\text{Topology optimization:} \quad \varepsilon = \varepsilon_{opt} \tag{10}$$

$$\text{Shape optimization:} \quad D = \psi \times D \tag{11}$$

2.3. Boundary Conditions

2.3.1. Fluid Transport

At the inlet of the manifold, a Dirichlet boundary condition[56,57] is set for the velocity. The inlet velocity is calculated using a prescribed flow rate and the cross-sectional area of the inlet channel. At the outlet of the manifold, a Neumann boundary condition[56,57] is applied for the velocity. The pressure is fixed to zero at the outlet and a Neumann condition is set at the inlet.

2.3.2. Species Transport

The concentration c is representative of either VO^{2+} or VO_2^+ during charging or discharging operation. The concentration field is initialized with 0 mol m^{-3} as well as the inlet concentration. At the outlet, a Neumann boundary condition is applied for the concentration. The maximum concentration is chosen to 100 mol m^{-3} for a straightforward analysis of the conversion.
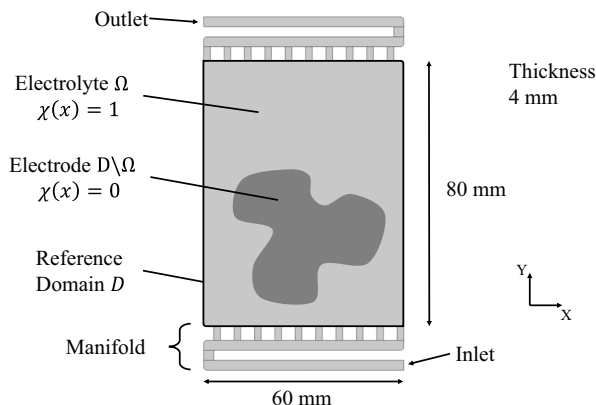

Figure 1. Computational domain of the 2D homogenized cell-scale model including inlet and outlet manifold. Additionally, the reference domain D and its subset domains Ω and D/Ω used in topology optimization are indicated.

2.4. Simulation Parameters

The default set of parameters used in the simulations is summarized in **Table 1** and **2**.

2.5. Computational Domain

The modeled domain represents a typical, experimental flow-through lab-scale cell, as illustrated in Figure 1. This design is chosen as it allows for experimental validation and was used in previous simulation studies[58] and experiments.[59,60] It incorporates a primary manifold at both the inlet and outlet of the electrode to ensure the uniform distribution of electrolyte. Detailed geometrical data are summarized in **Table 3**. The electrolyte flows through the cell from the bottom right (inlet) to the top left (outlet). The simulation mesh of the entire domain consists of about seventeen thousand triangle-dominated elements.

Table 1. Physical properties of the electrolyte and electrode.

Description	Symbol	Value	References
Electrolyte viscosity	μ	4.928×10^{-3} Pa s	[15]
Electrolyte density	ρ	1354 kg m^{-3}	[72]
Diffusivity VO^{2+} and VO_2^+	D_c	$3.9 \times 10^{-10} \text{ m}^2 \text{ s}^{-1}$	[15]
Maximum concentration	c_{max}	100 mol m^{-3}	Approximation
Fiber diameter	d_f	14×10^{-6} m	[73]
Active surface	A_V	$58\,471 \text{ m}^{-1}$	[73]

Table 2. Kinetic parameters of the reaction rate R_c.

Description	Symbol	Value	References
Mass transfer parameter	α	0.4	[55]
Mass transfer parameter	β	1.6×10^{-4}	[55]
Operating temperature	T	298 K	–

Table 3. Geometrical properties of the computational domain.

Description	Symbol	Value
Electrode height within the cell	h_c	80 mm
Electrode width within the cell	w_c	60 mm
Manifold channel width	w_m	3 mm
Thickness of distributor inlets	t_i	2 mm
Height of distributor inlets	h_i	4 mm
Number of distributor inlets	n_i	10
Height of vertical channel section	h_{vc}	3 mm
Gap between the respective inflow channels	$(w_c - w_m - n_i \times t_i)/(n_i - 1)$	mm
Radius of fillet	r_f	1 mm
Domain thickness	d_d	4 mm

3. Optimization Methodology

In this work, we adapt topology optimization to redistribute the porosity within the FB electrode and shape optimization to find optimized parameters of novel cell designs. In both scenarios, the goal is to minimize pressure drop while simultaneously maximizing the reaction rate to identify a favorable compromise between these contrasting factors. Typically, pressure drop is minimized at high porosity levels resulting from reduced flow resistance. In contrast, the reaction rate tends to increase with decreasing porosity driven by the increase in surface area. It is important to note that this assumption does not hold true for all porous media, but rather when electrode properties such as fiber diameter are kept constant. In the following section, the cost functional of the minimization problem and the optimization methodologies are explained.

3.1. Optimization Problem and Cost Functional

A generic formulation of the flow optimization problem is given according to

$$\text{find control } \gamma \text{ and state } f \text{ which} \\ \text{minimize } \mathcal{J}(f,\gamma) \text{ and fulfill } \mathcal{G}(f,\gamma) = 0 \tag{12}$$

Here, the function γ is referred to as the control of the optimization, the function f as the state of the model, the functional $\mathcal{J}$ as the objective or cost functional, and $\mathcal{G}(f,\gamma) = 0$ as the constraint or side condition. The side condition is presented by the governing equations in Section 2.2. The objective is formulated as a multiobjective cost functional to simultaneously minimize the inverse reaction rate of concentration and the pressure loss within the cell. According to Oleson et al.[61] the relation of inlet and outlet pressure is not a well-posed optimization function. Instead, the total viscous power dissipation ϕ_{diss} is used and defined as

$$\phi_{\text{diss}} = \int_D \tau : \mathbf{S} \, dV \tag{13}$$

where τ is the viscous stress and $\mathbf{S}$ is the strain rate tensor. The multiobjective functional $\mathcal{J}$ is

$$\mathcal{J} = \int_D s_1 \frac{1}{R_c} + s_2 \, \phi_{\text{diss}} \, dV \tag{14}$$

where s_1 and s_2 are scaling factors for each part of the cost functional. FBs encounter two primary challenges: Power loss stem from electrolyte pumping and incomplete conversion of active materials during operation. To address these problems, the flow resistance must be reduced by using highly porous electrodes. In contrast, large active surface area is necessary at the same time to achieve complete conversion. Within this model, the inversely proportional relationship between porosity and active surface area underscores the trade-off inherent in FBs, delineating two conflicting optimization objectives. To pinpoint an optimal solution, these quantities are integrated into a single multiobjective cost function. Each quantity is accompanied by a scaling factor, possessing inverse units of the reaction rate and power dissipation, respectively, to ensure compatibility. The scaling factors not only facilitate the combination of disparate metrics but also offer the flexibility to weight each quantity as needed within the optimization process. In this stage of research, the scaling factors are initially set to unity as a starting point. The functional $\mathcal{J}$ is used in both topology and shape optimization.

3.2. Topology Optimization Method

Use of topology optimization in this work is inspired by the research of Yaji et al.[18,31] where it is used to identify optimized flow field designs aiming to maximize the generation rate of species. As previously highlighted, the primary objective of this study is to determine the optimal porosity distribution within the electrode. The method aims at finding the optimal placement of material and void points within a specified domain, relying on finite-element discretization. The characteristic function $\chi(\mathbf{x})$ is

$$\chi(\mathbf{x}) = \begin{cases} 1 & \text{if } \mathbf{x} \in \Omega \\ 0 & \text{if } \mathbf{x} \in D \backslash \Omega \end{cases} \tag{15}$$

where $\mathbf{x}$ is the position in the reference domain D and Ω is the subset of material points as shown in Figure 1. The discontinuous function $\chi(\mathbf{x})$ of the density topology optimization approach[62] is replaced by a continuous function $0 \leq \theta(\mathbf{x}) \leq 1$ to enable differentiation. The optimization process is mesh dependent due to the allocation of values within the finite-element domain. To address this issue and to ensure the smoothness of $\theta(\mathbf{x})$, filtering techniques like the Helmholtz filter, which relies on partial differential equations, are employed.[63]

$$\theta_f = \theta_c + R_{\min}^2 \nabla^2 \theta_f \tag{16}$$

θ_f is the filtered material volume factor, θ_c is the raw control variable modified by the optimizer, and $R_{\min}$ is the filter radius to control the degree of regularization. Use of Helmholtz filtering can lead to a gray scale with no distinct physical meaning. To prevent the emergence of gray scale within the design domain, a smooth step function, known as projection, is formulated.

$$\theta = \frac{\tanh\big(\beta_o(\theta_f - \theta_\beta)\big) + \tanh\big(\beta_o\theta_\beta\big)}{\tanh\big(\beta_o(1 - \theta_\beta)\big) + \tanh\big(\beta_o\theta_\beta\big)} \tag{17}$$

where β_o is the projection slope and θ_β is the projection point. In the density approach, interpolation functions are used to penalize intermediate values of the material volume factor. Furthermore, Darcy's interpolation for fluid problems[64] is used in this work.

$$\theta_P = q \frac{1 - \theta}{q + \theta} \tag{18}$$

where θ_p is the penalized material volume factor and q is a parameter for controlling the damping of intermediate design variables. Unless otherwise stated, the parameters in **Table 4** are used to run the topology optimization calculations.

ADVANCED
SCIENCE NEWS
www.advancedsciencenews.com

Energy Technology
Generation, Conversion, Storage, Distribution
www.entechnol.de

Table 4. Topology optimization parameters.

Description	Symbol	Value
Filter radius	$R_{\min}$	0.001
Projection slope	β_o	8
Projection point	θ_β	0.5
Initial material volume factor	θ_0	0.5
Darcy penalization factor	q	1

Consequently, the optimization problem is formulated as

$$\underset{\theta}{\text{minimize}} \, \mathcal{J} \quad \text{subject to} \quad 0 \leq \theta(\mathbf{x}) \leq 1 \; \forall \mathbf{x} \in D \tag{19}$$

To connect mathematical optimization with the physics of the underlying model, the penalized material volume factor is used to parameterize porosity and active surface. In this work, we adapt the ansatz of Roy et al.[36] and Olesen et al.[61] and write the porosity and active surface as

$$\varepsilon_{\text{opt}} = \theta_P(\varepsilon_{\max} - \varepsilon_{\min}) + \varepsilon_{\min} \tag{20}$$

$$A_{V,\text{opt}} = A_V(1 - \varepsilon_{\text{opt}}) \tag{21}$$

where ε_{opt} is the optimized porosity, $\varepsilon_{\max}$ and $\varepsilon_{\min}$ are the porosity limits, and $A_{V,\text{opt}}$ is the optimized active surface. The choice of appropriate porosity limits is an important decision in terms of optimization, which is explained in detail in Section 5.1. The optimized quantities are used within the physical model.

By way of example, **Figure 2** shows the topology optimization history with the cost functional value and average porosity over the iteration number. In this case, the average porosity of the whole electrode domain is depicted. Selected topology designs are shown for iteration numbers 5, 10, 20, and 30.
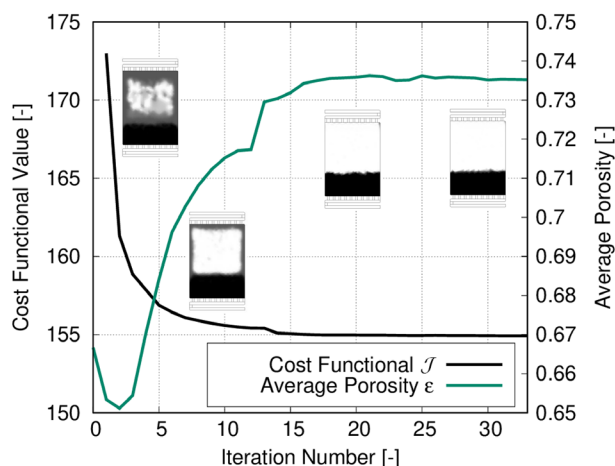

Figure 2. Cost functional and averaged porosity versus the iteration numbers of the topology optimization process. Topology designs of the porosity distribution for iteration numbers 5, 10, 20, and 30.

3.3. Shape Optimization

In shape optimization, the targeted quantity is scaled by the control variable. In this context, the parameters subject to optimization include the height or both height and width of the rectangular cell, the upper width of the trapezoidal cell, and the angle of the radial cell. The control variable undergoes variations within a constrained parameter space using the Nelder–Mead method[65] until an optimal value minimizing the cost functional is achieved. For a specific control variable, denoted as ψ, the optimization problem is formulated as follows.

$$\underset{\psi}{\text{minimize}} \, \mathcal{J} \quad \text{subject to} \quad \psi_{\min} \leq \psi \leq \psi_{\max} \tag{22}$$

where $\psi_{\min}$ and $\psi_{\max}$ are restrictions of the control variable. The actual bounds and initial values of the respective control variables are presented in Section 6. It should also be mentioned that in this investigation the porosity of the electrode is kept uniform.

3.4. Computational Information

Physical modeling and optimization calculations are implemented in COMSOL Multiphysics software version 6.1 using the laminar flow, transport of diluted species, topology optimization, and optimization interfaces. The software uses the finite-element method. Topology optimization is conducted using the gradient-based SNOPT algorithm,[66] while the convergence criterion is set to 1×10^{-6}. Topology optimization time is around 5–10 min on a simulation computer using an AMD Ryzen 9 3900X 12-core processor with 3.79 GHz and 64 GB RAM. The calculation time of a parameter sweep in shape optimization is around 20 min using a convergence criterion of 1×10^{-6} as well. During the geometric adaptations, the domain is remeshed.

4. Experimental Validation

The model is validated against experimentally determined open-circuit voltage (OCV) and combined half-cell potentials during charge. In the experimental setup, individual half-cell potentials are measured using reference electrodes. The VRFB consists of a $40 \, \text{cm}^2$ cell with an anion-exchange membrane (Fumasep FAP-450, FUMATECH BWT GmbH, Bietigheim-Bissingen, Germany) and GFA6 graphite felt (SGL Carbon GmbH, Meitingen, Germany) as electrodes (see ref. [59,60] for more details). The total vanadium concentration is 1.6 M and the tank volume is 60 mL each. The flow rate is 80 mL min^{-1} and current density is 25 mA cm^{-2}. To compare the conversion of active species within the model and the measured voltages in the experiment, a modified Nernst equation is used[67]

$$E_N = E^0 + \frac{RT}{zF} \times \ln\frac{1 - \text{SOC}}{\text{SOC}} \tag{23}$$

where E_N is the Nernst potential, E^0 the standard redox potential, R is the universal gas constant, T is the temperature, z is the number of transferred electrons, F is the Faraday constant, and SOC is the state of charge. The standard redox potentials for the positive and negative half cells are 1.004 and -0.255 V,

**ADVANCED
SCIENCE NEWS**

www.advancedsciencenews.com

Energy Technology
Generation, Conversion, Storage, Distribution
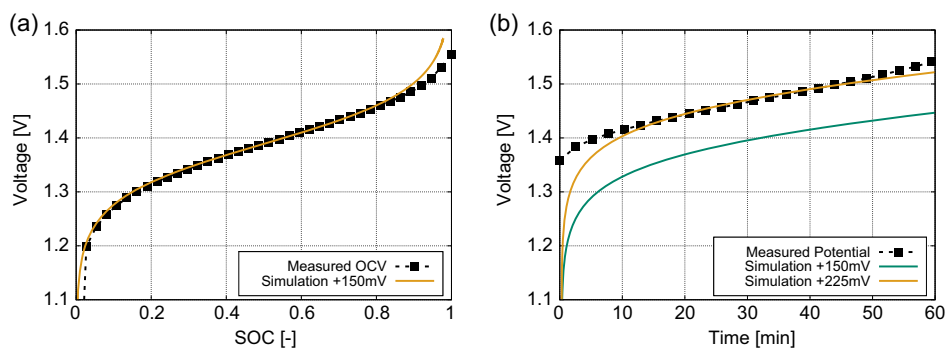
www.entechnol.de

Figure 3. Experimental validation of the underlying modeling approach. a) Open-circuit cell voltage as a function of the state of charge. Additional 150 mV is included in the simulation to fit the experimental data. b) Combined half-cell potentials over time during charge operation. No membrane potential considered. Additional 75 mV is included in the simulation result to address overpotentials that the model does not inherently capture.

respectively. A transient simulation approach is adapted to cover the charging process. **Figure 3**a depicts the OCV plotted against SOC for both experimental and simulated data. The experimental curve represents the OCV of the entire cell. In contrast, the simulation curve is derived by combining the half-cell potentials. Additionally, an extra 150 mV is incorporated to fit the experimental curve. According to Knehr et al.[68] a discrepancy of around 130–140 mV between experiment and VRFB model arises because of the incomplete description of the electrochemical double layer using Nernst equation. Further differences arise due to the usage of SOC instead of activities and the neglect of junction potentials. Overall, there is a remarkable alignment between the curves, showcasing a minor deviation of ≈2.6% at the highest SOC.

In Figure 3b, the charging process of the VRFB over time is presented. Here, the experimental curve represents the summation of individual half-cell potentials without considering the membrane potential. The simulated curve is depicted in green. Here, the previously mentioned 150 mV are incorporated as well. To replicate the charging behavior observed in the experiment, the reaction parameters α and β (as seen in Equation (9)) are adjusted to 1.37 and 8×10^{-6}, respectively. Additionally, the outlet concentration is aligned with the inlet to reflect the electrolyte's circulation. Notably, the Nernst equation shown does not encompass any overpotentials inherent in the charging process. The reasons for these overpotentials include, among others, activation, contact resistance, or the conductivity of the electrolyte. To compensate for these overpotentials, an increment of 75 mV is additionally introduced to the simulation curve (orange), resulting in a good conformity with the experimental data. The overall voltage correction is hence 225 mV. The root mean square error between the experiment and simulation is 0.03, with a maximum deviation of about 10% observed during the initial stages.

5. Results of Topology Optimization

5.1. Porosity Intervals

In general, porosity values range between 0 and 1, where zero represents a solid material with no void spaces and one signifies complete void space. To explore optimization characteristics in this study, three distinct porosity intervals are employed for the electrode. In order to cover a broad spectrum of potential values, the first range selected extends from 0.05 to 0.95. Expanding the interval further is computationally unfeasible. Considering FBs, electrode porosity values typically tend to fall within the upper third. Consequently, this study takes into consideration the intervals of 0.7–0.95 and 0.6–0.8. **Figure 4** shows the optimization results of the three intervals for flow rates of 10 mL min^{-1} (top row) and 25 mL min^{-1} (bottom row). For the largest interval, porosity varies in an unstructured manner. Given the interval's magnitude, optimization has to cope with an extensive design space, posing challenges in identifying an optimal minimum. As the flow rate increases, flow resistance becomes more important. Consequently, porosity values are higher at elevated flow rates to minimize energy dissipation. This correlation is represented by a lighter shade of gray. For the constrained intervals, a clearer porosity distribution results. While the interval of 0.7–0.95 still exhibits irregularities at its upper end, a lower porosity downstream of the inlet manifold is obtained consistently for all illustrated cases. This observation agrees with the experimental findings of Yoon et al.[69] where a similar design resulted in improved energy efficiency. Additionally, it can be noticed that the area of reduced porosity downstream of the inlet decreases with higher flow rates to mitigate energy losses due to flow resistance.

5.2. Flow Rate Comparison

Figure 5 illustrates the horizontal mean porosity along the electrode height for different flow rates and the three porosity intervals. **Table 5** shows the investigated flow rates and the corresponding mean velocities within the electrode. In this comparison, the distribution of the actual porosity value along the flow direction is analyzed in more detail. Indeed, as observed previously, lower flow rates tend to correspond to lower porosity levels in general. In the case of the highest investigated flow rate (100 mL min^{-1}), the porosity tends to approach or reach the maximum value within the specified interval. The porosity distribution at lower flow rates generally exhibits a consistent pattern: Toward the lower section of the electrode, close to the inlet, a
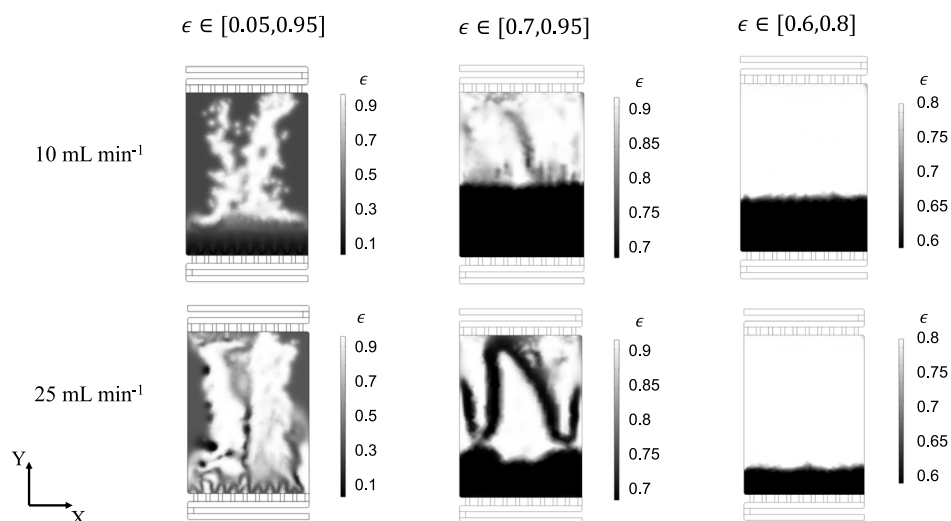
ADVANCED
SCIENCE NEWS
www.advancedsciencenews.com

Energy Technology
Generation, Conversion, Storage, Distribution
www.entechnol.de

Figure 4. Results of the topology optimization using different porosity intervals and flow rates. The top row corresponds to a flow rate of 10 mL min⁻¹ and the bottom row to 25 mL min⁻¹.
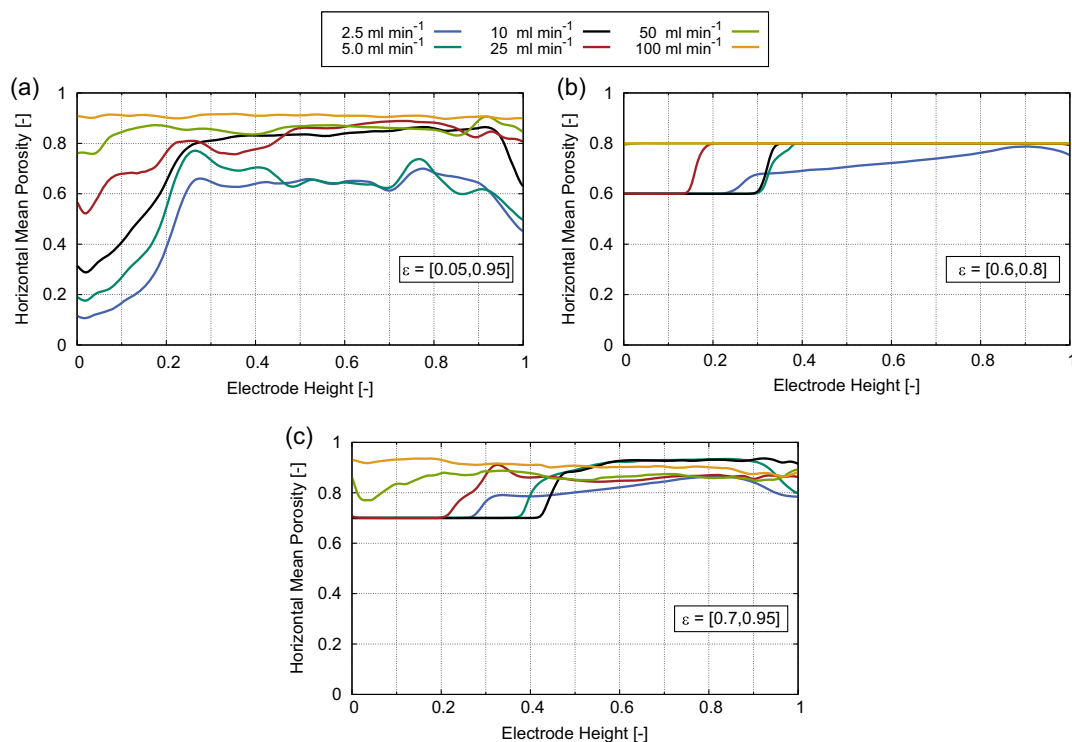

Figure 5. Horizontal mean porosity resulting from topology optimization versus the normalized electrode height. Comparison of different flow rates for the combined optimization. The subfigures show different porosity intervals: a) $\varepsilon \in [0.05, 0.95]$, b) $\varepsilon \in [0.6, 0.8]$, c) $\varepsilon \in [0.7, 0.95]$.

preference for low porosity and subsequent larger active surface area is observed. With an increase in electrode height, the porosity typically experiences a sudden and pronounced increase. In the further course, it then either tends to the maximum value of the interval or remains in the range of high values. Under certain conditions, a porosity distribution with lower values downstream of the inlet and higher values infront of the outlet may be beneficial. Experimental studies have additionally demonstrated that an increase in porosity within the electrode downstream can result in enhanced energy efficiency.[69,70] This design offers a large active area in the region of high reactant concentration and enhances mass transport of the product. When comparing the different intervals, it becomes evident that porosity exhibits more pronounced fluctuations with larger interval sizes.

Table 5. Flow rates and corresponding flow velocities within the electrode.

Flow rate [mL min^{-1}]	Flow speed [ms^{-1}]
2.5	1.76×10^{-4}
5	3.60×10^{-4}
10	6.89×10^{-4}
25	1.72×10^{-3}
50	3.50×10^{-3}
100	7.05×10^{-3}

The increased design freedom associated with longer intervals can explain these fluctuations. When the optimization is subject to tighter constraints, as observed in the case of $\varepsilon \in [0.6, 0.8]$, the transition between low and high porosity becomes more distinct and evident. This is promising, because such a distribution is more likely to be feasible in real-world applications.

5.3. Performance Comparison of Homogeneous and Two-Part Electrodes

In this section, homogeneous electrodes, each possessing the maximum and minimum porosity values within their respective intervals, are compared to an optimized two-part design. From the practical perspective, implementation of the two-part electrode design is most feasible. It consists of denser material with lower porosity in the lower 20% of the electrode height (see Figure 4 bottom right). The porosities are homogeneous and the flow rate is 25 mL min^{-1}. Comparison of performance is based on pressure drop (Δp), integrated reaction rate (R_c), and rate of conversion (RoC). The RoC is a physical measure to describe the conversion efficiency of active material within the electrode and is defined as

$$\text{RoC} = \frac{c_{\text{outlet}}}{c_{\text{max}}} \tag{24}$$

where c_{outlet} is the average concentration at the outlet of the domain. **Figure 6** shows the performance comparison using the values of intervals $\varepsilon \in [0.6, 0.8]$ (left) and $\varepsilon \in [0.7, 0.95]$ (right). The results of the electrode with minimum porosity
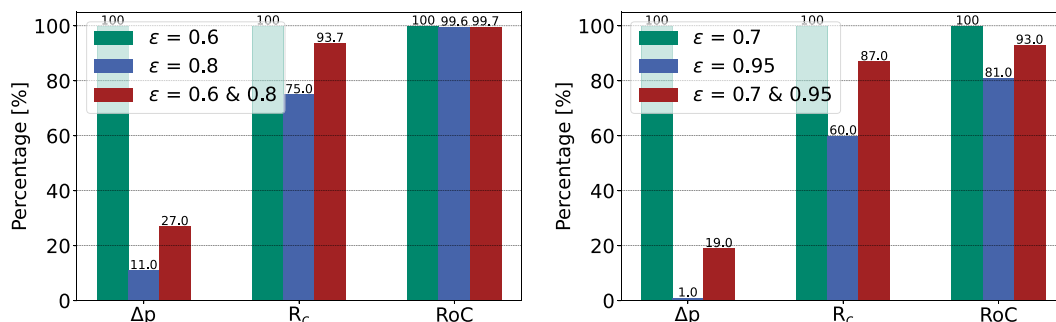
are shown in green and set to 100% for better comparison of the different physical quantities. The electrodes of maximum porosity and made of two parts are shown in blue and red, respectively.

In terms of pressure drop and reaction rate, the anticipated outcomes of both diagrams are in agreement with our findings. As regards the pressure drop, both the higher-porosity and the two-part electrode configurations demonstrate an increase by reduced flow resistance. It is noted that this enhancement is more pronounced with higher porosity values. However, the reaction rate shows a decrease with higher porosity for the two-part electrode configuration due to the reduced active surface area. With regard to the RoC, our analysis reveals intriguing findings. For the porosity values of 0.6 and 0.8, the RoC remains nearly consistent for all three electrodes. The actual RoC of $\varepsilon = 0.06$ reaches 99%, indicating the nearly complete conversion of active material. Consequently, favoring the highest porous electrode ($\varepsilon = 0.8$) would be ideal due to the energy saved when pressure drop is reduced. In contrast, for porosity values of 0.7 and 0.95, the actual RoC at $\varepsilon = 0.7$ also reaches 99%. However, both studied electrodes exhibit a lower RoC in comparison. As a result, it can be deduced that in this scenario, the two-part electrode configuration is preferable. Despite the acceptable reduction in RoC of around 7%, it reduces pressure loss by 81% compared to $\varepsilon = 0.7$, making it a more advantageous choice. This comparison underscores that an optimized design may not necessarily align with practical applicability. Moreover, the outcome of optimization is largely dependent on specific electrode parameters, such as porosity or active surface area, along with operational factors like flow rate.

5.4. Topology Optimization Using Novel Cell Designs

In order to investigate the behavior of topology optimization in different cell geometries, three additional designs according to Gurieff et al.[17] are examined. **Figure 7** shows the designs of horizontal, trapezoidal, and radial shape. The porosity interval is $\varepsilon \in [0.7, 0.95]$ and the flow rate is 2.5 mL min^{-1} in this example. The different designs show optimization results similar to those of the previously described vertical cell. In a horizontal design, the cell exhibits a wider width than height, while in a vertical design, the cell displays a greater height than width. **Figure 8** highlights the horizontal mean porosity over the
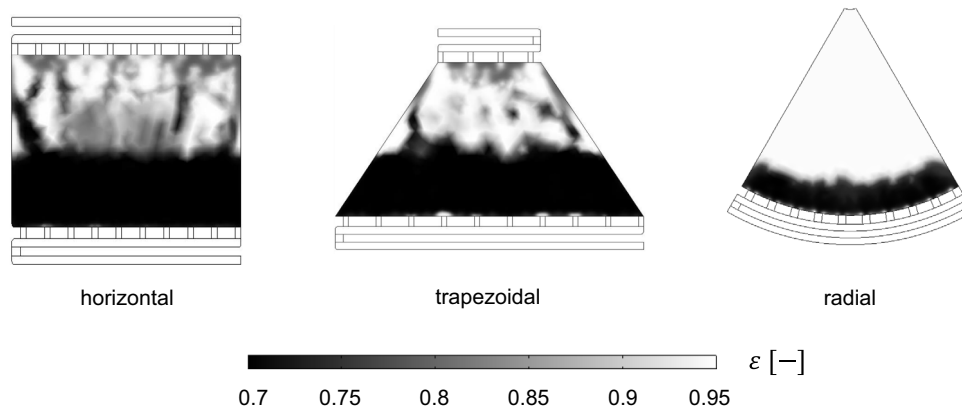

Figure 6. Performance comparison of electrodes with homogeneous single-porosity and two-part porosity in terms of pressure drop (Δp), reaction rate (R_c), and RoC. The two-part electrode configuration has the lower porosity value within the initial 20% of the electrode height downstream of the inlet manifold. The electrode porosities are 0.6 & 0.8 (left) and 0.7 & 0.95 (right).

**ADVANCED
SCIENCE NEWS**

www.advancedsciencenews.com

Energy Technology
Generation, Conversion, Storage, Distribution

www.entechnol.de

Figure 7. Different flow battery cell designs according to studies from Gurieff et al.[17] Within the electrodes, the porosity distribution is shown for $\varepsilon \in [0.7, 0.95]$ and 2.5 mL min^{-1}.
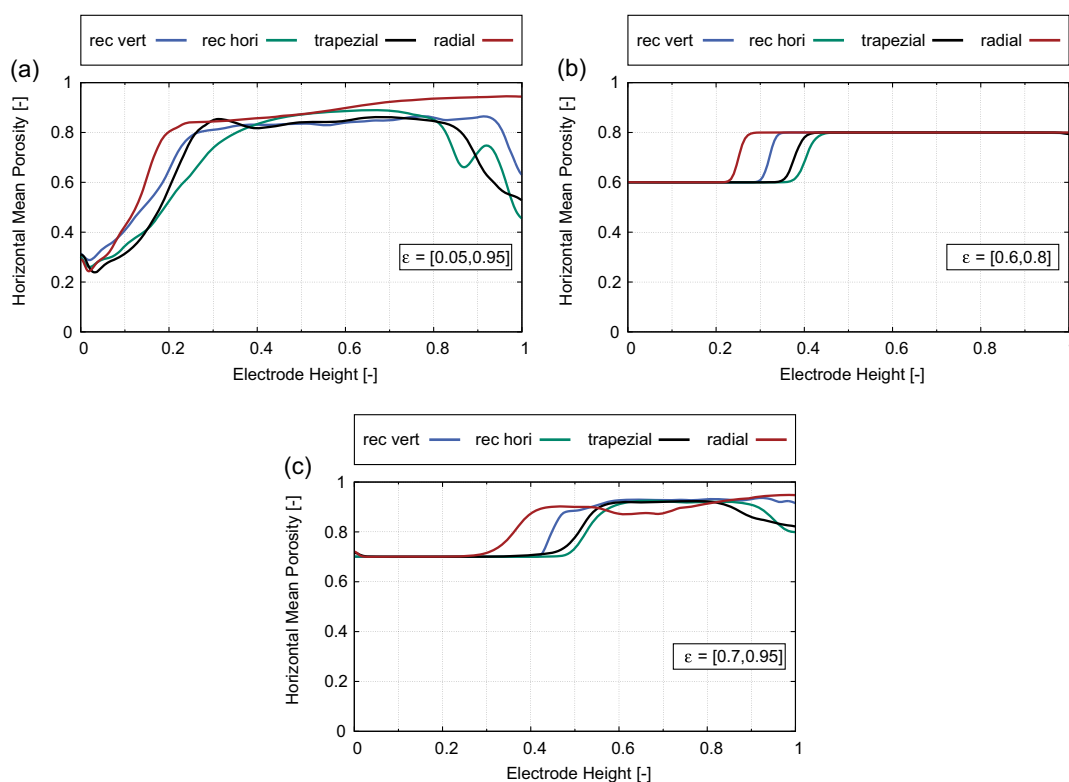

Figure 8. Comparison of different cell designs, with horizontal mean porosity plotted versus normalized electrode height. The subfigures show the different porosity intervals: a) $\varepsilon \in [0.05, 0.95]$, b) $\varepsilon \in [0.6, 0.8]$, c) $\varepsilon \in [0.7, 0.95]$. The flow rate is 10 mL min^{-1}.

electrode height for the different designs and intervals. The default design rec vert of previous investigations is included for comparison. The flow rate is 10 mL min^{-1}. We observe low-porosity values downstream of the inlet, with values gradually ascending toward higher levels as we approach the outlet. Within the broadest porosity interval, $\varepsilon \in [0.05, 0.95]$, porosity exhibits a moderate overall increase in spite of fluctuations and decreases near the outlet. These variations may be attributed to the greater design freedom resulting from the broader interval. When considering narrower porosity intervals, by contrast,

porosity initially remains at its minimum value and then experiences a rapid and pronounced increase to the maximum. This transition is more pronounced within the smallest interval and occurs at lower heights. A comparison of various design configurations reveals that the transition occurs earliest in the radial design. This can be attributed to the increased flow velocity near the outlet, resulting from the narrowed cross section. As regards the different flow rates, the behavior is in agreement with that described in Section 5.2, where porosity tends to approach the maximum value as the flow rate increases.

6. Results of Shape Optimization

This research centers on the optimization of geometric parameters for cell design. In particular, optimization covers the cell's height, the ratio of its height to width, and the ratio between the top and bottom widths of the cell. Moreover, the angle is adjusted in the radial design. Throughout this investigation, the porosity of the electrode remains uniform and the same. The cost functional is the same as in topology optimization. In the study, flow rates between 5 and 100 mL min^{-1} are investigated in a porosity range of 0.6–0.95 due to practical feasibility.

6.1. Rectangular Cell Design

For the optimization of the default rectangular cell design, **Table 6** presents details regarding the initial value and the optimization bounds. For height optimization, the initial height and width are set to 80 and 60 mm, respectively. Throughout the optimization process, the control variable ψ is adjusted within the specified bounds until the cost functional reaches its minimum, while keeping the width of the cell constant. In case of the height-to-width ratio optimization, the initial values of height and width are the same, whereas the width of the cell is varied simultaneously within the given bounds using a second control variable λ. The height is thus optimized between 4 and 200 and the width between 30 and 120 mm. **Figure 9** shows the results of the height (a) and height-to-width optimization (b) versus porosity for different flow rates. For height optimization, it can be stated that the lower the porosity is, the more optimal it is to have a shorter cell. A reduced cell height leads to a lower pressure drop and in the case of low porosity, it ensures a sufficiently long residence time for the effective conversion of active material. As porosity increases, the optimal height increases as well, reflecting a
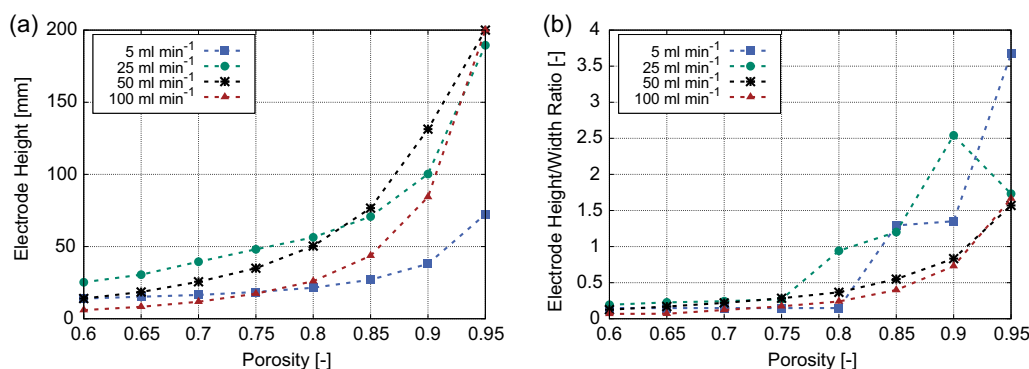
reduced impact of pressure drop and a need for more space to achieve complete conversion. This behavior is consistent for all flow rates. At higher flow rates, however, the increase in optimal height is more pronounced. This steep increase is attributed to the exponential relationship between pressure drop and porosity. Additionally, it is crucial to point out that the maximum is attained for the two highest flow rates. When optimizing both height and width concurrently, a similar pattern results. Within the porosity range of 0.6–0.8, the height-to-width ratio remains below one, suggesting a preference for a broader design. In this range, the emphasis is on minimizing pressure loss. As porosity continues to rise, the height-to-width ratio increases as well. At the two highest flow rates, the increase is exponential, because the maximum width is reached at every optimization. Therefore, the only option is to increase the height to enhance the reaction rate. Fluctuations observed at lower flow rates are caused by the fact that neither the height nor the width approaches the defined bounds. This indicates that the intuitive vertical format commonly used in many cells may not be the optimal shape and needs to be reconsidered.

6.2. Trapezoidal and Radial Cell Designs

In **Table 7**, the optimization parameters are presented for both the trapezoidal and radial designs. For the trapezoidal design, the bottom width is fixed at 120 mm, while the top width is adjusted within the range from 40 to 120 mm. In the case of the radial design, the initial angle of 60° between the two sides is varied within the range of 30–90°. The graphs in **Figure 10** show the optimization results of the top-to-bottom-width ratio of the trapezoidal design (a) and the angle of the radial design (b) versus porosity for different flow rates. Optimization calculations for the trapezoidal design were carried out successfully for the cases

Table 6. Optimization of the initial rectangular cell design.

Optimization	Height	Height-to-width ratio
Height	$\psi \times 80$ mm	$\psi \times 80$ mm
Width	60 mm	$\lambda \times 60$ mm
Bounds height	$0.05 < \psi < 2.5$	$0.05 < \psi < 2.5$
Bounds width	–	$0.05 < \lambda < 2.5$

Table 7. Optimization of the initial rectangular cell design.

| Optimization	Trapezoidal	Radial
Top width	$\psi \times 40$ mm	–
Bottom width	120 mm	–
Angle	–	$\psi \times 60°$
Bounds	$1.0 < \psi < 3.0$	$0.5 < \psi < 1.5$

Figure 9. Shape optimization of the default rectangular cell design. The diagrams show a) optimized height and b) height-to-width ratio versus porosity for different flow rates.
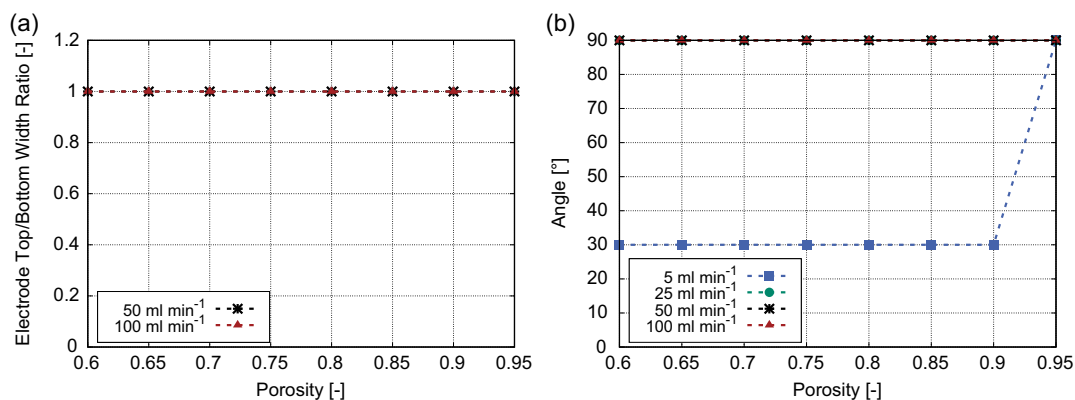
Figure 10. Shape optimization of the trapezoidal and radial cell designs. The graphs show the a) optimal top-to-bottom-width ratio and the b) optimized angle versus porosity for different flow rates.

of 50 and 100 mL min^{-1} only, which is due to numerical limitations. The consistent top-to-bottom-width ratio of one over all porosities suggests a preference for a rectangular design. This preference is driven by the objective to minimize pressure loss, as the tapering profile of the trapezoid leads to increased flow velocities. The optimal angle of the radial design tends to the maximum of 90° for all flow rates regardless of porosity. This design offers a larger surface area for the conversion of active species and pressure drop is reduced as the cross section increases. An exception is found in the curve for 5 mL min^{-1}. In this case, the optimal angle remains at the minimum of 30° and sharply rises to the maximum at the highest porosity investigated. In this flow regime, the reduction of pressure loss with increasing cross-section is not significant. Moreover, the reaction rate is sufficient to convert all species, which makes an increase in active area unnecessary.

7. Conclusion

This study introduces a comprehensive modeling and optimization framework for a VRFB, which combines both topology and shape optimization approaches. The topology optimization method redistributes porosity within the FB electrode, providing a novel perspective for re-evaluating its design properties. Concurrently, shape optimization optimizes the cell geometry parameters for innovative cell designs, with the cost functional aimed at minimizing pressure drop while maximizing the reaction rate. The underlying model incorporates the Brinkmann-type Navier–Stokes equations with permeability determined by the Carman–Kozeny equation and transport of diluted species. Reaction kinetics focus on single-species conversion, employing a simplified reaction term based on the mass transfer coefficient. Model parameters are validated using separate half-cell potentials from an experimental cell design. Using a modified Nernst equation and mass transfer correlation parameters, the model successfully predicts OCV measurements and charging behavior.

Topology optimization over various porosity ranges and flow rates reveals the expected dependence on selected porosity intervals. The optimization demonstrates a preference for a porosity

distribution with lower values and subsequent larger surface area downstream of the inlet when pressure drop and reaction rate are optimized simultaneously. At this point, it is important to mention that in this work a linear relationship between porosity and active surface is assumed. Indeed, there are many porous electrode materials with different, nonlinear relationships between their porosity and active surface. As flow rates increase, overall porosity tends to be higher to compensate for the energy loss due to the elevated pressure differential. The transition between high and low porosity is also influenced by the flow rate. Implementing the two-part design yields acceptable conversion rates with a significantly reduced pressure drop, although each individual case must be considered. This work underscores the importance of a comprehensive optimization framework for enhancing the efficiency and design adaptability of FBs.

Regarding the results in the Appendix, gradient-based topology optimization shows the expected dependence on the initial value. The sanity check of individual optimization of target variables confirms the expected results, with maximum porosity values for pressure drop optimization and minimum values for reaction rate optimization. A sensitivity study highlights the significant influence of viscosity, in addition to reaction rate parameter α and flow rate, on porosity distribution. In terms of FB performance, it is found that the flow rate and all reaction rate parameters are crucial to achieve optimal conversion rates.

In addition, we explored further innovative cell designs for their optimization potential. Apart from the original rectangular format, we investigated horizontal, trapezoidal, and radial designs. Regarding topology optimization, the behavior was similar to that observed previously. Once again, lower porosity was preferred downstream of the inlet. In comparison, the radial design exhibited a much earlier transition to lower porosities in flow direction due to higher velocities resulting from the smaller cross-section. In the course of shape optimization, we optimized the height and height-to-width ratio of the original design. It became evident that with increasing porosity and a fixed width, the electrode height increased. Investigations with a flexible height and width revealed a preference for the horizontal format for cells with a porosity of less than 0.9. Examination of

ADVANCED
SCIENCE NEWS
www.advancedsciencenews.com

Energy Technology
Generation, Conversion, Storage, Distribution

www.entechnol.de

the trapezoidal design revealed a consistent preference for a rectangular design for the parameters used. For the radial design, optimization almost always produced the maximum angle. In both cases, the reduction of pressure loss by expanding the cross-section was decisive. In summary, shape optimization reveals that the intuitively assumed vertical format is not necessarily the optimal choice for cell design. A more detailed investigation, including experimental studies, is imperative to identify the optimal design and remains the subject of ongoing research.

In a rigorous evaluation, it is imperative to delineate the limitations of both the model and the optimization process. To enhance the model for more robust optimization outcomes in future, various pathways for improvement can be explored. Primarily, the inclusion of the Butler–Volmer kinetics deserves attention, as it offers a more precise depiction of the active material conversion. This inclusion also provides the opportunity to optimize electrochemical variables, such as voltage or current. Additionally, the determination of the cost functional involves contemplating on the weighting of individual terms. Conducting a parameter study in this context would yield insights into their optimal weighting. Furthermore, the assumption of a linear inverse relationship between porosity and active surface, as stated in Equation (21), requires further discussion. Experimental investigations have revealed the trapezoidal design's reduced concentration polarization.[50] Employing shape optimization with electrochemical parameters could facilitate the trade-off between pressure loss and this polarization, potentially identifying an optimal ratio between the top and bottom width.

In conclusion, this article has contributed to advancing the optimization methods for FB cells. Despite the need for further refinement, the simplicity of the presented model provides a flexible optimization framework applicable to various systems. The incorporation of a multiobjective cost functional and the exploration of porosity distribution have pushed the state of research in this field. Importantly, our findings challenge the intuitive assumption that the vertical format of the cell is the optimal design. This work represents a significant step forward, offering valuable insights and paving the way for future improvements in the optimization of FB cells.

Appendix

A1 Mesh Independence

The half-cell geometry is discretized into numerous mesh elements. In order to ensure that the simulation results are independent of the number of elements used, a mesh independence test is conducted. The study maintains consistent simulation conditions for all cases, with the only variation being the number of mesh elements used. **Figure A1** presents the pressure drop between inlet and outlet (Δp), the integrated reaction rate (R_c), and the mean porosity versus the number of mesh elements of the electrode. Regarding the results in Figure A1a, no topology optimization is conducted, while in Figure A1b, the three distinct porosity intervals are chosen. Since porosity is defined within the electrode only, both diagrams indicate the number of elements of the electrode. The mesh independence study encompasses seven different meshes, each with an increasing number of elements, to thoroughly evaluate the impact of mesh refinement on the results. As observed, the results exhibit a significant variation when considering simulations using the first three meshes. To achieve independent results, a mesh containing at least 8.314 elements is required. The relative error between the mesh with 8,314 elements and that with 18 530 elements is consistently below 1% for all parameters, except for the porosity interval $\varepsilon \in [0.05, 0.95]$, where the error reaches 4%. Due to this observation and the considerably higher computational costs associated with finer meshes, the grid comprising 8314 electrode elements is selected. This choice results in a total of 17 198 mesh elements for the whole geometry.

A2 Influence of the Initial Value

The choice of the initial value in topology optimization with gradient-based solvers plays a crucial role and can have significant effects on the outcome of the optimization process. Gradient-based optimization algorithms aim to minimize the cost functional, but they can end up in different local minima depending on the chosen starting position. A well-chosen initial value can increase the likelihood of finding a global minimum or a better
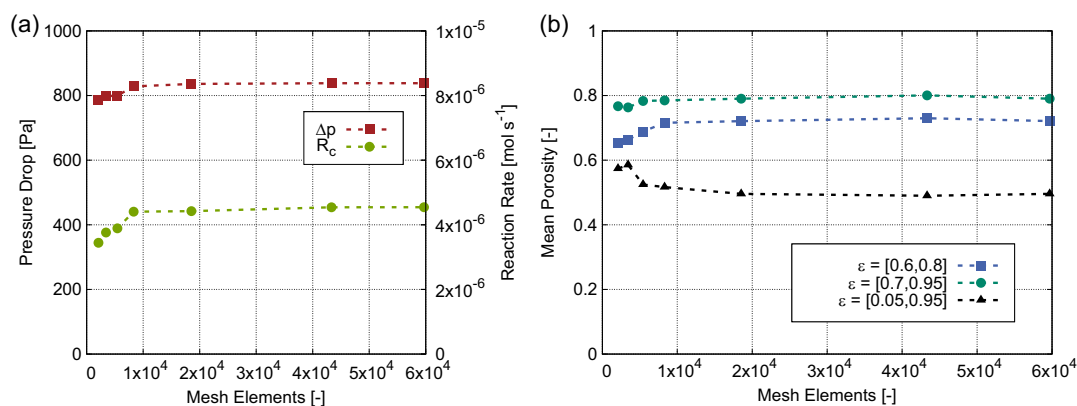

Figure A1. a) Pressure drop between inlet and outlet and integrated reaction rate R_c versus mesh elements of the electrode domain. b) Mean porosity of the electrode versus mesh elements resulting from topology optimization. Three different porosity intervals are displayed.

**ADVANCED
SCIENCE NEWS**

www.advancedsciencenews.com

Energy Technology
Generation, Conversion, Storage, Distribution

www.entechnol.de

local minimum. Furthermore, the selection of the initial porosity distribution at the outset of the optimization has an impact on the convergence behavior, which, in turn, affects the final result. To examine the influence of the initial value of the penalized material volume factor on porosity distribution, **Figure A2** shows six graphs of the horizontal mean porosity as a function of the normalized electrode height for three porosity intervals $\varepsilon \in [0.05, 0.95]$ (top), $\varepsilon \in [0.6, 0.8]$ (middle), $\varepsilon \in [0.7, 0.95]$ (bottom) and two flow rates $2.5\,\mathrm{mL\,min^{-1}}$ (left) and $25\,\mathrm{mL\,min^{-1}}$ (right). In this instance, porosity is displayed as an average for horizontal slices and subsequently graphed relative to electrode height. In each plot, every curve represents a porosity distribution calculated with a varying initial value (θ_0) ranging from 0 to 1. The initial value of the starting porosity can be determined using θ_0 and Equation (20). The key in Figure A2d applies to all subfigures.

The larger the porosity range, the more distinct the solutions appear to be for different initial values. A clear dependence of porosity fluctuations on the choice of the initial value is not found. For the largest interval (Figures A2a and A2b), the solutions exhibit substantial variability, making it challenging to make unequivocal statements about trends. In principle, higher porosity values are generally preferred and these tend to increase with higher flow rates, which is attributed to the increasing influence of pressure drop. The smallest interval (Figures A2c and A2d) yields the smallest deviations in porosity distribution. For $25\,\mathrm{mL\,min^{-1}}$, the curves of different initial values closely overlap, whereas at $2.5\,\mathrm{mL\,min^{-1}}$, discrepancies become more pronounced, especially in the upper third of the electrode. Here, the influence of the initial value is marginal. Within the interval $\varepsilon \in [0.7, 0.95]$ (Figures A2e and A2f), characterizing the diverse
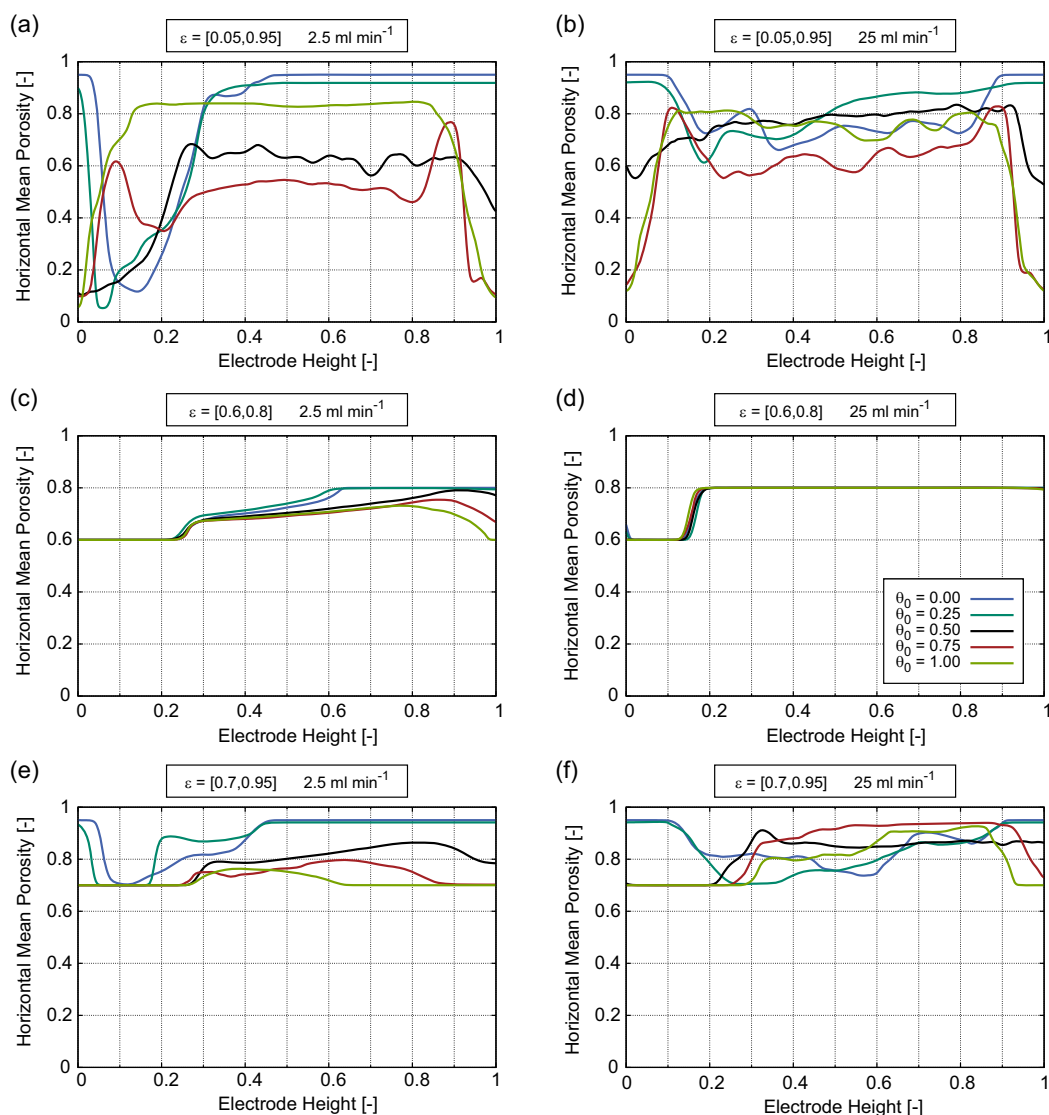

Figure A2. Influence of different initial values θ_0 of the optimization penalization factor on porosity distribution. Different porosity intervals $\varepsilon \in [0.05, 0.95]$ (top), $\varepsilon \in [0.6, 0.8]$ (middle), $\varepsilon \in [0.7, 0.95]$ (bottom) and flow rates $2.5\,\mathrm{mL\,min^{-1}}$ (left) and $25\,\mathrm{mL\,min^{-1}}$ (right) are depicted. The graphs show horizontal mean porosity as a function of the normalized electrode height. The key in subfigure d) holds for all subfigures.

**ADVANCED
SCIENCE NEWS**

www.advancedsciencenews.com

Energy Technology
Generation, Conversion, Storage, Distribution

www.entechnol.de

solutions proves to be challenging. The previously described pattern of low porosity in the lower region and high porosity in the upper region of the electrode is partly true only. For initial values of 0 and 0.25, high porosity is observed in the lower region, while the trend in porosity distribution remains discernible for the remaining initial values. In conclusion, it can be confirmed that the initial value and optimization constraints have a significant influence on the solution. A parameter space has been identified where the solution is largely independent of the initial value.

A3 Sanity Check: Single- and Multiobjective Cost Functional

To investigate the effect of optimization with a combined and separate cost functional, identical optimization calculations are carried out for reaction rate and pressure drop individually and in combination. This is done for different flow rates and the previously described porosity intervals. **Figure A3** shows the mean porosity of individual and combined optimization versus the flow rate for different intervals. It is evident from individual optimization results that porosity tends to approach either the minimum or maximum value within the defined interval. The reason is that the lowest pressure drop is attained by maximizing porosity, thereby reducing flow resistance. Conversely, when optimizing solely for the reaction rate, the minimum porosity value is favored due to the increased active surface area, which enhances the reaction. The linear inverse relationship between the quantities arises from Equation (20) and (21). This behavior is mostly independent of the applied flow rate, except for comparatively small rates. This may be due to a sufficient residence time at small flow rates. The combined optimization yields a rise in mean porosities as the flow rate increases, ultimately trending toward the upper limit of the interval at the

highest flow rates. This trend is primarily driven by the increased significance of pressure loss minimization as the flow rate increases. It is important to note that the two components of the cost functional are equally weighted in this context. When comparing the three different porosity intervals, it becomes apparent that the individual values exhibit a greater range within larger intervals. This phenomenon can be attributed to the increased design freedom resulting from the broader porosity range.

A4 Sensitivity Analysis

To investigate the influence of the respective model parameters on performance and on topology optimization, a sensitivity analysis is conducted. For this purpose, the elementary effect method is employed.[71] This method is a local sensitivity measurement, often referred to as the one-at-a-time (OAT) measurement. It evaluates partial derivatives to determine how variations of one factor of the input parameters $(X_1, X_2, \ldots, X_k)$ affect the model output $Y(X_1, X_2, \ldots, X_k)$ while keeping all other factors constant at a nominal value. The elementary effect $d_i^{(j)}(\mathbf{X})$ is defined as

$$d_i^{(j)}(\mathbf{X}) = \frac{\mathbf{Y}(X_1, \ldots, X_{i-1}, X_i + \Delta, X_{i+1}, \ldots, X_k) - \mathbf{Y}(X_n)}{\Delta} \quad (A1)$$

where the first part in the numerator represents the model output moved OAT of a step Δ in the inputs' domain and $\mathbf{Y}(X_n)$ is the output at nominal values of all parameters. The amount of steps is j. To characterize the sensitivity of the input parameters, the average μ_i and standard deviations σ_i of the respective elementary effects are determined according to
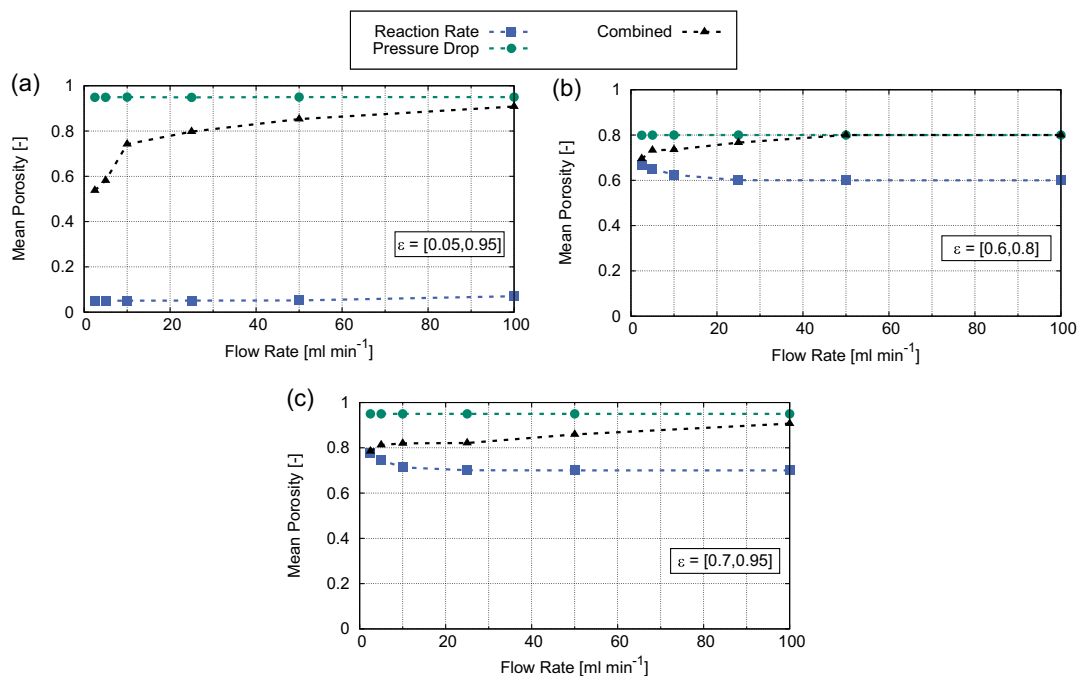

Figure A3. Mean porosity resulting from topology optimization versus flow rate. Comparison of topology optimizations for pressure drop and reaction rate and combined multiobjective optimization. The subfigures show different porosity intervals: a) $\varepsilon \in [0.05, 0.95]$, b) $\varepsilon \in [0.6, 0.8]$, c) $\varepsilon \in [0.7, 0.95]$.

**ADVANCED
SCIENCE NEWS**

www.advancedsciencenews.com

Energy Technology
Generation, Conversion, Storage, Distribution

www.entechnol.de

$$\mu_i = \frac{1}{r} \sum_{j=1}^{r} d_i^{(j)}(\mathbf{X}), \quad \sigma_i = \sqrt{\frac{1}{r} \sum_{j=1}^{r} \left(d_i^{(j)}(\mathbf{X}) - \mu_i \right)^2} \qquad (A2)$$

In the so-called Morris plane, the standard deviation is plotted against the average value. High values of the average indicate high influential parameters and high values of the standard deviation indicate nonlinear and/or interacting parameters. In order to characterize the input parameters influence on the optimization result, the coefficient of variation (CoV) is defined as the ratio of the standard deviation and the average of the optimized porosity distribution within the electrode.

$$\mathrm{CoV} = \frac{\sigma\left(\varepsilon_{\mathrm{opt}}\right)}{\mu\left(\varepsilon_{\mathrm{opt}}\right)} \qquad (A3)$$

It is a measure to characterize the variation of porosity relative to the mean. The physical input parameters are documented in **Table A1** with their nominal values as well as reasonable ranges. The nominal value is positioned at the midpoint of the interval. Each parameter range is subdivided into seven values, including

both the nominal and the extreme values. These divisions are linear for all parameters except for diffusivity, for which an exponential division is employed. The simulations adhere to the OAT methodology, with one parameter altered at a time while the others are kept constant at their nominal values. This procedure yields a total of 189 simulations covering nine physical parameters, each tested with seven values at three porosity intervals. Consequently, 18 elementary effects can be derived for each parameter.

The results of the sensitivity analysis are depicted in **Figure A4** showing the standard deviation versus the average value of the elementary effects for both CoV (left) and RoC (right). For the CoV, the order of influence is as follows: $T < \rho < D < A_V < \beta < c_{\max} < \mu < \dot{V} \ll \alpha$. Temperature, density, and diffusivity are found at the lower end, indicating their limited impact on the optimization process. In general, the temperature and density range is quite narrow in FBs due to the essential presence of liquid water. Diffusivity in the porous media hardly has any influence on pressure drop and reaction rate. Parameters associated with the reaction rate exert a somewhat higher influence, followed by viscosity and flow rate. The latter factors are directly connected with the pressure drop and play a crucial role in the optimization process. It is interesting to see that the reaction parameter α has the highest influence. Although the optimization is dominated by the minimization of pressure loss especially at high flow rates, the reaction term still has a decisive influence. The order of parameters influencing the RoC is as follows: $T \ll \rho < c_{\max} < \mu, D \ll \dot{V} < A_V, \beta < \alpha$. In this modeling approach, temperature does not exert any influence on the reaction. For this reason, it is not represented on the Morris plane. Similarly to the CoV results, density and diffusivity have a low impact on RoC. Compared to the other reaction rate parameters, the maximum concentration influences the RoC only slightly. The flow rate has a higher influence due to its impact on the residence time of the active material. In summary, the study provides a qualitative statement with respect to the influence of the model parameters only. Yet, it allows for a good assessment of the importance of individual parameters. This should be taken into consideration when designing cells and electrodes.
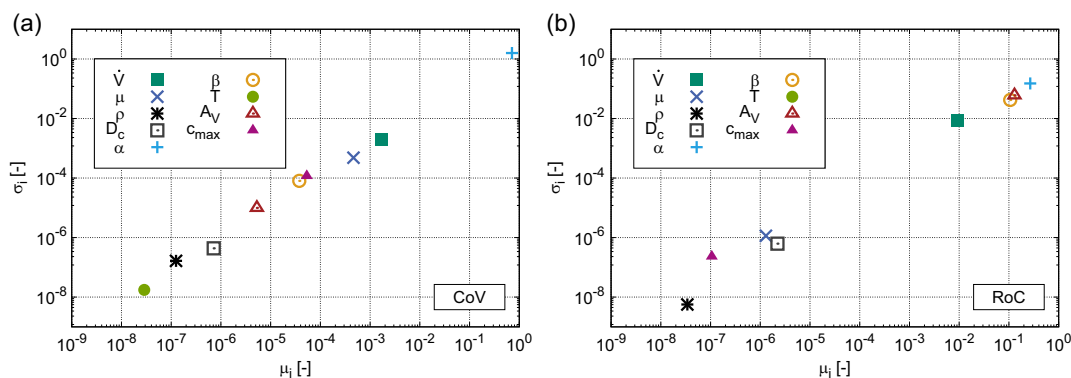
Table A1. Nominal input parameters and ranges of variation for sensitivity analysis.

Parameter	Symbol	Unit	Nominal	Range	References
Flow rate	$\dot{V}$	$\mathrm{mL\,min^{-1}}$	51.25	[2.5,100]	[74]
Viscosity	μ	Pa s	5.5×10^{-3}	[0.001,0.01]	[37]
Density	ρ	$\mathrm{Kg\,m^{-3}}$	1075	[950,1200]	[72]
Diffusivity	D_c	$\mathrm{m^2\,s^{-1}}$	5×10^{-10}	$[10^{-11},10^{-8}]$	Estimation
Mass transfer parameter	α	–	1.05	[0.1,2.0]	Estimation
Mass transfer parameter	β	–	5.5×10^{-4}	$[10^{-4},10^{-3}]$	Estimation
Temperature	T	K	325.5	[298,353]	Estimation
Specific area	A_v	$\mathrm{m^{-1}}$	2.55×10^5	$[10^4, 5 \times 10^5]$	[35]
Maximum concentration	$c_{\max}$	$\mathrm{mol\,m^{-3}}$	1550	[100,3000]	[75]

Figure A4. Representation of the sensitivity analysis in the Morris plane showing the standard deviation (σ_i) over the mean value (μ_i) of the respective elementary effects. High values on the *x*-axis indicate high influential parameters, while high values on the *y*-axis indicate nonlinear and/or interacting parameters. a) The Morris plane of the elementary effects on the CoV. b) The Morris plane of the elementary effects on the RoC.

Conflict of Interest

The authors declare no conflict of interest.

Data Availability Statement

The data that support the findings of this study are available from the corresponding author upon reasonable request.

[1] S. Chu, Y. Cui, N. Liu, *Nat. Mater.* **2017**, *16*, 16.

[2] T. M. Gür, *Energy Environ. Sci.* **2018**, *11*, 2696.

[3] J. Noack, N. Roznyatovskaya, T. Herr, P. Fischer, *Angew. Chem., Int. Ed.* **2015**, *54*, 9776.

[4] M. Park, J. Ryu, W. Wang, J. Cho, *Nat. Rev. Mater.* **2016**, *2*, 16080.

[5] S. Kim, E. Thomsen, G. Xia, Z. Nie, J. Bao, K. Recknagle, W. Wang, V. Viswanathan, Q. Luo, X. Wei, A. Crawford, G. Coffey, G. Maupin, V. Sprenkle, *J. Power Sources* **2013**, *237*, 300.

[6] E. Sánchez-Díez, E. Ventosa, M. Guarnieri, A. Trovò, C. Flox, R. Marcilla, F. Soavi, P. Mazur, E. Aranzabe, R. Ferret, *J. Power Sources* **2021**, *481*, 228804.

[7] Y. Zeng, T. Zhao, L. An, X. Zhou, L. Wei, *J. Power Sources* **2015**, *300*, 438.

[8] M. Rychcik, M. Skyllas-Kazacos, *J. Power Sources* **1988**, *22*, 59.

[9] Z. Huang, A. Mu, L. Wu, B. Yang, Y. Qian, J. Wang, *ACS Sustainable Chem. Eng.* **2022**, *10*, 7786.

[10] B. Khaki, P. Das, *Electrochim. Acta* **2022**, *405*, 139842.

[11] A. Shah, M. Watt-Smith, F. Walsh, *Electrochim. Acta* **2008**, *53*, 8087.

[12] H. Al-Fetlawi, A. Shah, F. Walsh, *Electrochim. Acta* **2009**, *55*, 78.

[13] H. Al-Fetlawi, A. Shah, F. Walsh, *Electrochim. Acta* **2010**, *55*, 3192.

[14] A. A. Shah, R. Tangirala, R. Singh, R. G. A. Wills, F. C. Walsh, *J. Electrochem. Soc.* **2011**, *158*, A671.

[15] D. You, H. Zhang, J. Chen, *Electrochim. Acta* **2009**, *54*, 6827.

[16] X. Ma, H. Zhang, F. Xing, *Electrochim. Acta* **2011**, *58*, 238.

[17] N. Gurieff, C. Cheung, V. Timchenko, C. Menictas, *J. Energy Storage* **2019**, *22*, 219.

[18] K. Yaji, T. Yamada, S. Kubo, K. Izui, S. Nishiwaki, *Int. J. Heat Mass Transfer* **2015**, *81*, 878.

[19] F. Wandschneider, D. Finke, S. Grosjean, P. Fischer, K. Pinkwart, J. Tübke, H. Nirschl, *J. Power Sources* **2014**, *272*, 436.

[20] O. Sigmund, K. Maute, *Struct. Multidiscip. Optim.* **2013**, *48*, 1031.

[21] J. D. Deaton, R. V. Grandhi, *Struct. Multidiscip. Optim.* **2014**, *49*, 1.

[22] Y. Luo, O. Sigmund, Q. Li, S. Liu, *Addit. Manuf.* **2022**, *55*, 102795.

[23] R. Behrou, K. Kirsch, R. Ranjan, J. K. Guest, *Comput. Methods Appl. Mech. Eng.* **2022**, *389*, 114270.

[24] A. T. Gaynor, T. E. Johnson, *Addit. Manuf.* **2020**, *33*, 101149.

[25] J. Alexandersen, C. S. Andreasen, *Fluids* **2020**, *5*, 29.

[26] I. Aramendia, U. Fernandez-Gamiz, A. Martinez-San-Vicente, E. Zulueta, J. M. Lopez-Guede, *Energies* **2021**, *14*, 176.

[27] C. Kim, H. Sun, *Int. J. Automot. Technol.* **2012**, *13*, 783.

[28] R. Behrou, A. Pizzolato, A. Forner-Cuenca, *Int. J. Heat Mass Transfer* **2019**, *135*, 72.

[29] Q. Li, Y. Duan, D. Chai, X. Zhang, X. Min, G. Li, *Int. J. Energy Res.* **2021**, *45*, 3214.

[30] Z. Zhang, J. Zhang, T. Zhang, *Sustainability* **2022**, *14*, 8.

[31] K. Yaji, S. Yamasaki, S. Tsushima, T. Suzuki, K. Fujita, *Struct. Multidiscip. Optim.* **2018**, *57*, 535.

[32] C.-H. Chen, K. Yaji, S. Yamasaki, S. Tsushima, K. Fujita, *J. Energy Storage* **2019**, *26*, 100990.

[33] V. A. Beck, J. J. Wong, C. F. Jekel, D. A. Tortorelli, S. E. Baker, E. B. Duoss, M. A. Worsley, *J. Power Sources* **2021**, *512*, 230453.

[34] N. Gilmore, A. Hassanzadeh-Barforoushi, V. Timchenko, C. Menictas, *Appl. Therm. Eng.* **2021**, *183*, 116227.

[35] Q. He, J. Yu, Z. Guo, J. Sun, S. Zhao, T. Zhao, M. Ni, *e-Prime Adv. Electr. Eng. Electron. Energy* **2021**, *1*, 100001.

[36] T. Roy, M. A. Salazar de Troya, M. A. Worsley, V. A. Beck, *Struct. Multidiscip. Optim.* **2022**, *65*, 171.

[37] T. Y. Lin, S. E. Baker, E. B. Duoss, V. A. Beck, *J. Electrochem. Soc.* **2022**, *169*, 050540.

[38] P. Charoen-amornkitt, M. Alizadeh, T. Suzuki, S. Tsushima, *Int. J. Heat Mass Transfer* **2023**, *202*, 123725.

[39] J. Wang, X. Liu, Y. Wang, *Chem. Eng. J.* **2023**, *458*, 141420.

[40] A. Tang, J. Bao, M. Skyllas-Kazacos, *J. Power Sources* **2014**, *248*, 154.

[41] A. Forner-Cuenca, F. R. Brushett, *Curr. Opin. Electrochem.* **2019**, *18*, 113.

[42] X. Guan, M. Skyllas-Kazacos, C. Menictas, *Batteries* **2023**, *9*, 7.

[43] E. Prumbohm, G. D. Wehinger, *Chem. Ing. Tech.* **2019**, *91*, 900.

[44] C. T.-C. Wan, R. R. Jacquemond, Y.-M. Chiang, A. Forner-Cuenca, F. R. Brushett, *Energy Technol.* **2023**, *11*, 2300137.

[45] Z. Huang, A. Mu, L. Wu, H. Wang, *J. Energy Storage* **2022**, *45*, 103526.

[46] G. Xiao, G. Yang, S. Zhao, L. Xia, F. Chu, Z. Tan, *Energy* **2022**, *258*, 124757.

[47] M. Wu, T. Zhao, R. Zhang, H. Jiang, L. Wei, *Energy Technol.* **2018**, *6*, 333.

[48] N. Gurieff, D. F. Keogh, M. Baldry, V. Timchenko, D. Green, I. Koskinen, C. Menictas, *Appl. Sci.* **2020**, *10*, 8.

[49] M. D. R. Kok, A. Khalifa, J. T. Gostick, *J. Electrochem. Soc.* **2016**, *163*, A1408.

[50] M. Yue, Q. Zheng, F. Xing, H. Zhang, X. Li, X. Ma, *AIChE J.* **2018**, *64*, 782.

[51] J. Bear, *Dynamics of Fluids in Porous Media*, Number Parts 1-2 in Dynamics of Fluids in Porous Media, American Elsevier Publishing Company, Chicago, USA, **1972**.

[52] K. Yazdchi, S. Srivastava, S. Luding, E. Oñate, D. Owen, *Particle-Based Methods II - Fundamentals and Applications* **2011**.

[53] M. W. Verbrugge, R. F. Hill, *J. Electrochem. Soc.* **1990**, *137*, 886.

[54] Q. Xu, T. Zhao, *Phys. Chem. Chem. Phys.* **2013**, *15*, 10841.

[55] D. Schmal, J. Van Erkel, P. J. Van Duin, *J. Appl. Electrochem.* **1986**, *16*, 422.

[56] O. C. Zienkiewicz, R. L. Taylor, P. Nithiarasu, *The Finite Element Method for Fluid Dynamics*, 7 ed., Butterworth-Heinemann, Oxford, UK **2013**.

[57] M.-M. Maubourguet, J.-M. Tanguy, *Finite Differences*, John Wiley & Sons, Ltd., Hoboken, New Jersey **2010**, pp. 95–107, Ch. 6, ISBN 9781118557877.

[58] A. Wolf, E. Baudrin, H. Nirschl, *Energy Technol.* **2023**, *11*, 2300175.

[59] N. Roznyatovskaya, T. Herr, M. Küttinger, M. Fühl, J. Noack, K. Pinkwart, J. Tübke, *J. Power Sources* **2016**, *302*, 79.

[60] J. N. Noack, L. Vorhauser, K. Pinkwart, J. Tuebke, *ECS Trans.* **2011**, *33*, 3.

[61] L. H. Oleson, F. Okkels, H. Bruus, *Int. J. Numer. Methods Eng.* **2006**, *65*, 975.

[62] M. P. Bendsøe, O. Sigmund, *Topology Optimization by Distribution of Isotropic Material*, Springer Berlin Heidelberg, Berlin, Heidelberg **2004**, pp. 1–69, ISBN 978-3-662-05086-6.

[63] B. S. Lazarov, O. Sigmund, *Int. J. Numer. Methods Eng.* **2011**, *86*, 765.

[64] T. Borrvall, J. Petersson, *Int. J. Numer. Methods Fluids* **2003**, *41*, 77.

[65] J. A. Nelder, R. Mead, *Comput. J.* **1965**, *7*, 308.

[66] P. E. Gill, W. Murray, M. A. Saunders, *SIAM Rev.* **2005**, *47*, 99.

[67] J. Geiser, H. Natter, R. Hempelmann, B. Morgenstern, K. Hegetschweiler, *Z. Phys. Chem.* **2019**, *233*, 1695.

[68] K. Knehr, E. Kumbur, *Electrochem. Commun.* **2011**, *13*, 342.

[69] S. J. Yoon, S. Kim, D. K. Kim, *Energy* **2019**, *172*, 26.

[70] W. Chen, J. Kang, *Chem. Phys.* **2020**, *529*, 110577.

[71] M. D. Morris, *Technometrics* **1991**, *33*, 161.

[72] A. Tang, S. Ting, J. Bao, M. Skyllas-Kazacos, *J. Power Sources* **2012**, *203*, 165.

[73] A. Wolf, S. Kespe, H. Nirschl, *Pore-Scale Modeling of Flow Batteries*, John Wiley & Sons, Ltd. **2023**, pp. 413–442, Ch. 18, ISBN 9783527832767.

[74] N. Roznyatovskaya, J. Noack, H. Mild, M. Fühl, P. Fischer, K. Pinkwart, J. Tübke, M. Skyllas-Kazacos, *Batteries* **2019**, *5*, 13.

[75] S. Roe, C. Menictas, M. Skyllas-Kazacos, *J. Electrochem. Soc.* **2015**, *163*, A5023.